Blanchet, C. L., Osborne, A. H., Tjallingii, R., Ehrmann, W., Friedrich, T., Timmermann, A., Brückmann, W., Frank, M. (2021): Drivers of river reactivation in North Africa during the last glacial cycle. - Nature Geoscience, 14, 97-103.

https://doi.org/10.1038/s41561-020-00671-3

Drivers of river reactivation in North Africa during the last glacial cycle

Authors:

Cécile L. Blanchet[1*], Anne H. Osborne[2], Rik Tjallingii[3,1], Werner Ehrmann[4], Tobias Friedrich[5], Axel Timmermann[6,7], Warner Brückmann[2], Martin Frank[2]

Affiliations:

1: Helmholtz Centre Potsdam GFZ, Section Climate Dynamics and Landscape Evolution, Telegrafenberg, 14473 Potsdam, Germany

2: GEOMAR Helmholtz Centre for Ocean Research Kiel, Wischhofstraße 1-3, 24148 Kiel, Germany

3: Royal Netherlands Institute for Sea Research NIOZ, Department Ocean Systems, De Landsdiep 4, 1797 SZ 't Horntje (Texel), The Netherlands

4: University Leipzig, Institute for Geophysics and Geology, Talstraße 35, 04103 Leipzig, Germany

5: Department of Oceanography, School of Ocean and Earth Sciences and Technology, University of Hawaii at Mānoa, 1000 Pope Road, Marine Science Building (MSB) 205, Honolulu, HI 96822, USA

6: Center for Climate Physics, Institute for Basic Science (IBS), Busan, South Korea

7: Pusan National University, Busan, South Korea

* Corresponding author

Keywords

Hydroclimates, Sahara, palaeo-rivers, sediment provenance, radiogenic isotopes, clay minerals, grain size, Gulf of Sirte, migration corridors

Abstract

North African greening phases, during which large rivers ran through the Sahara Desert, occurred repeatedly during the Quaternary and are regarded as key periods for the development of past human populations. However, the timing and mechanisms responsible for the reactivation of the presently dormant fluvial systems remain highly uncertain. Here we present hydroclimate changes over the past 160,000 years, reconstructed from analyses of the provenance of terrestrial sediments in a marine sediment record from the Gulf of Sirte (offshore Libya). By combining high-resolution proxy data with transient Earth system model simulations, we are able to identify the various drivers leading to the observed shifts in hydroclimate and landscapes. We show that river runoff occurred during warm interglacial phases of MIS5 and MIS1 due to precession-forced enhancements in summer and autumn rainfall over the entire watershed, feeding presently dry river systems and intermittent coastal streams. In contrast, shorter-lasting and less intense humid events during glacial stages MIS3 and MIS4 were related to autumn and winter precipitation over the Libyan coastal regions that were driven by Mediterranean storms. Our results reveal large shifts in hydroclimate environments during the last glacial cycle, which likely exerted a strong evolutionary and structural control on past human populations, potentially pacing their dispersal across northern Africa.

Main

Humid phases have repeatedly turned the presently hyper-arid Sahara Desert into a green haven for both large vertebrates and human populations in the geological past[1]. Palaeo-environmental reconstructions revealed the presence of fauna and flora typical of Sahelian grasslands (e.g., giraffes, elephants, hippopotamuses) in the core of the current desert[1–3]. The occupation of northern Africa by various populations of *Homo sapiens* since about 300,000 years[4] highlights the importance of this region for prehistoric population dynamics[5]. The near-periodic occurrence of humid phases in northern Africa has been linked to orbitally-paced strengthening and northward migration of the African monsoon system[6–8]. High-latitude climatic regimes have also exerted a significant control on north African climates, as documented by co-occurrence of arid periods in the Sahel and North-Atlantic Heinrich events[9] and by intervals of enhanced winter precipitation in the northern African coastal regions[8,10,11]. The role of seasonality of precipitation and moisture sources on the hydrological balance of northern Africa during the Late Quaternary still remains uncertain[8,12,13]. By combining proxy data with modelling experiments, we provide new insights into the timing and underlying processes causing past river runoff at the nowadays dry coast of northern Africa. The goal of our study is to better constrain palaeo-hydrological and palaeo-landscape changes in this region.

The Gulf of Sirte as a recorder of North African hydroclimates

The Gulf of Sirte (GS) is a key location for reconstructing hydroclimatic variations in northern Africa and for investigating teleconnections between low- and high-latitude climate processes. At present, the coastal regions of northern Africa receive up to 300 mm/yr of precipitation, mostly during winter from Mediterranean storm tracks (Fig. 1). Summer precipitation is limited to the northernmost boundary of the African monsoon at ~20º N (Extended data Fig. 1). The hyper-arid central Sahara separates these two

precipitation regimes and large perennial river systems, able to supply fluvial sediments to the GS, are currently absent (Fig 1). However, a dense network of fossil streams and rivers have been identified across the central Sahara using geomorphological and remote-sensing methods[1,14,15] (Fig. 1). The Sahabi and Kufrah palaeo-river systems originated in the Tibesti mountains and fed lakes and wetlands such as Lake Siwa in north-eastern Libya before discharging into the eastern GS[14]. The Irharhar palaeo-river system originated in the Hoggar mountains and fed Lake Chott-El-Jerid, which then discharged into the Gulf of Gabès[16].

Episodes of surface seawater freshening and sapropel formation have been identified in marine sediments from the southern Mediterranean during the early Holocene[17,18] and Marine Isotope Stage (MIS) 5e[19] and linked to reactivation of these palaeo-river systems (Fig. 1). However, there are currently no continuous sedimentary records from the GS that extend beyond 18 ka before present (BP)[18]. This has prevented establishing a precise timing of changes in fluvial dynamics and determining their forcing factors.

Here, we present records obtained from the upper 5 m of sediment core 64PE349-8 (33º35.145'N, 17º15.456'E, 2095 m water depth). This new record presents past sedimentary and hydroclimatic variations in the GS covering a full glacial-interglacial cycle (160 kyr). The chronology is based on radiocarbon dating, tephra chronology and correlation of the *Globigerinoides ruber* oxygen isotope record ($\delta^{18}O$, Fig.3a) to other regional records (see Methods). We identified four sapropel layers (S1, S3, S4 and S5), which were deposited during the interglacial summer insolation maxima of MIS1 and MIS5 (Extended data Fig. 2).

Tracking fluvial pulses

The reconstruction of hydroclimate and reactivation of North African palaeo-rivers is based on changes in the provenance and transport of detrital sediments to the GS. We use a

combination of radiogenic isotope signatures, grain-size distributions and clay mineralogy of the detrital sediment fraction to distinguish the input of aeolian dust and fluvial sediments.

Radiogenic neodymium (ε_{Nd}, see Methods) and strontium ($^{87}Sr/^{86}Sr$) isotope compositions of detrital particles and clay mineralogy are established provenance tracers, which have been successfully used for northern Africa and the Mediterranean Sea[9,20–22]. The radiogenic Nd and Sr isotope variability reflects lithology and age of the source rocks. Sediment and rock samples from Libyan and Algerian volcanic fields (including the Tibesti and Hoggar volcanic plateaus) are characterized by distinctly high ε_{Nd} and low $^{87}Sr/^{86}Sr$ signatures[19,23] (>5 and <0.710, resp.) (Fig. 1, 2a). In contrast, surface sediments from low-altitude basins located at the foothills of these volcanic plateaus are mostly derived from crystalline basements and have low ε_{Nd} and high $^{87}Sr/^{86}Sr$ signatures (<-12 and >0.714, resp.) (Fig. 1, 2a). Some of these basins have been identified as preferential dust sources (PDS) for aeolian particles deposited in Libya and the southern Mediterranean Sea[23,24]. Aeolian dust and marine surface sediments deposited in the dust-dominated regions of the Sahara and the North Atlantic show a crystalline-dominated ε_{Nd} signature (Extended data Fig. 1b). Clay minerals are diagnostic for specific weathering regimes of the parent rocks at the site of formation. North African aeolian dust is characterised by high abundances of kaolinite and palygorskite[9,17,22]. In contrast, surface sediments from Libyan volcanic source rocks are enriched in smectite[17,18,22].

In core 64PE349-8, changes in detrital sediment provenance are determined using the median values of radiogenic isotopes, clay minerals, and grain-size distributions for sapropel layers, non-sapropel sediments (NS) and glacial MIS 3 and 4 sediments (MIS3/4) (Fig. 2). NS sediments have a typical dust-dominated signature with median $^{87}Sr/^{86}Sr$ and ε_{Nd} values (~0.7185 and -12, resp.) similar to the isotopic signatures of northern and sub-Saharan PDS (Fig. 2b,c) and high proportions of kaolinite and palygorskite (Fig. 2d). In

contrast, sapropel sediments have significantly more radiogenic median ε_{Nd} values of ≥-11 and less radiogenic $^{87}Sr/^{86}Sr$ of ≤0.717 (Figs. 2a-c), accompanied by maximum median smectite contents (Fig. 2d). These geochemical and mineralogical signatures depict higher erosional contributions from Libyan volcanic fields and soils (Fig. 2a). Erosion products from the Nile river watershed and Sicily have similar radiogenic isotope signatures (Fig. 2a), but it was shown that these sources have not contributed to the sedimentary budgets in the GS[17,18]. Therefore, contributions with more radiogenic ε_{Nd} and less radiogenic $^{87}Sr/^{86}Sr$ signatures predominantly originated from the volcanic fields of Libya.

Dominant grain-size populations were identified using end-member modelling of detrital grain-size distributions, which are indicative for sediment transport mechanisms[25] (Methods). Most of the variance in the grain-size distribution for core 64PE849-8 can be explained by the interplay of 3 grain-size end-members with modes between 3 and 45 µm (Extended data Fig. 3). High proportions of the fine-grained end-member (EM1, mode = 3µm) occur in sapropel layers (Fig. 2e) and have been associated with river-transported sediments in the Mediterranean[22]. The detrital fractions in NS sediments are enriched in the coarser EM3 (mode = 45 µm) and correspond to grain-size distributions of aeolian dust collected in Libya and the southern Mediterranean[26,27].

River reactivation during interglacial precession minima

Volcanic-rich fine-grained sedimentation in core 64PE349-8 is diagnostic of large fluvial input to the GS and peaks during interglacial precession minima (IPM) associated with enhanced boreal summer insolation (Fig. 3). These episodes are fundamentally different from the present dust-dominated regime. Potential volcanic sources are located either in southern or in northern Libya but cannot be distinguished based on their radiogenic Nd and Sr isotope compositions (Fig. 1, Fig. 2a). We will therefore use evidence from other proxy records and modelling experiments to assess their contributions to the fluvial runoff.

146 The reactivation of the Sahabi, Kufrah and Irharhar palaeo-river systems required a
147 northward shift of the monsoon rainfall belt to approximately 25ºN. Palaeo-rainfall
148 estimations for the Hoggar and Tibesti mountains (20-25^{o}N) indicate >300 mm/yr during
149 past interglacials[2,13,28,29]. This amount was probably sufficient to reactivate the palaeo-river
150 systems in northern Africa, with the Irharhar operating as an intermittent summer stream
151 whereas the Sahabi and Kufrah were likely perennial rivers[30].
152 Transient simulations conducted with the LOVECLIM Earth system model[31] confirm these
153 results and yield mean annual precipitation rates (MAP) between 50 and 700 mm/yr
154 around a median of 60 mm/yr over the Tibesti (Fig. 3e). Prominent simulated MAP pulses
155 >300 mm/yr occur during IPM and they coincide with fluvial-rich sapropel layers of core
156 64PE349-8 (Fig. 3a-c). This confirms that the Sahabi and Kufrah rivers were important
157 contributors of freshwater and sediments to the GS. In LOVECLIM, most of the simulated
158 Tibesti precipitation during IPMs occurs in summer and early autumn (from July to
159 October, Fig. 4c,d) with large rainfall anomalies of up to 1500 mm in August (Extended
160 data Fig. 5c). Despite some discrepancies between the LOVECLIM present-day control
161 runs and observational data from the region (Extended data Fig. 5a and Methods), the
162 overall precipitation amount and seasonal ITCZ displacement is well-captured and in
163 agreement with proxy data[2,13,28]. The prominent summer precipitation anomaly over the
164 Tibesti derives from a reinforcement and northward displacement of the West African
165 summer monsoon and the associated rainfall belt (Fig. 4c).
166 At the Libyan coast, the simulated MAP varied between 250 and 400 mm/yr around a
167 median of 270 mm/yr, with higher values during IPM (Fig. 3e). During IPM, LOVECLIM
168 simulates more rainfall in autumn and winter as compared to today while summer
169 precipitation was slightly reduced (Fig. 4c,d and Extended data Fig. 5b,c). The synoptic
170 climatic conditions during rainfall maxima on the Libyan coast are very similar to those
171 identified at Lake Ohrid[32]. They depict enhanced moisture advection due to a southward

position of the Mediterranean storm tracks and enhanced cyclogenesis in the Mediterranean region (Fig. 4d), related the contraction of the Hadley cell and a stronger land-sea temperature contrast in autumn (with warmer sea surface temperatures)[32–34]. Because of the key position of the GS as a recorder of southern and northern climatic dynamics, we are able to confirm the reinforcement of both summer monsoon and autumn and winter Mediterranean rainfall regimes during IPM. We propose here that the entire watershed in Libya was activated during IPM, whereby the southern sources were dominant contributors to the runoff. Sensitivity simulations show that precipitation dynamics over the Tibesti are largely precession-driven, with Northern Hemisphere ice-sheet (NHIS) size and greenhouse gas concentrations further controlling the overall amplitude and the length of rainfall maxima (Extended data Fig. 6a-d). On the Libyan coast, MAP dynamics are partly driven by changes in the obliquity of the Earth's axis and by the NHIS size, which tends to delay the precipitation maxima during terminations and reduce their magnitude (Extended data Fig. 6e-h). The contribution from obliquity-forced MAP in northern Libya might explain the occurrence of a peak in freshwater release (traced by the $\delta^{18}O$ of foraminifera, Fig. 3a) shifted towards the top of the sapropel layers, especially during high-obliquity phases in S1 and S5. A full assessment of moisture source (e.g., externally-sourced vs. Mediterranean-sourced) of precipitation is however necessary to determine the potential effect of autumn-winter freshwater runoff on deep-water stagnation and sapropel formation[35].

A green coastal corridor during the last Glacial

In addition to the prominent sapropel layers, humid periods were also recorded in the GS during glacial stages MIS3 and MIS4. Sediment provenance reflects mixed volcanic and crystalline sources as suggested by intermediate median ε_{Nd}, $^{87}Sr/^{86}Sr$ and smectite values (Fig. 2b-d). Two main phases of higher fluvial runoff from volcanic terrains are

identified at 72-61 ka BP and 48-37 ka BP, characterized by finer sediments, more radiogenic ε_{Nd} and less radiogenic $^{87}Sr/^{86}Sr$ signatures (Fig. 3b,c).

Humid conditions have been detected in northern Libya and Tunisia during MIS3/4 and associated to Mediterranean-sourced moisture advected by winter storm tracks[10,12,16] (Fig. 3d). Lower MAP are simulated by LOVECLIM for both northern Libya and the Tibesti during glacial precession minima (GPM), with the contribution from coastal precipitation being dominant (Fig. 3e, 4e,f). This suggests that precipitation over the Tibesti and Hoggar plateaus was not sufficient to generate runoff to the GS and that most of the fluvial input derives from the activation of coastal wadis. Fluvial drainage of northern Libya would also result in a sediment mixture incorporating volcanic-derived as well as crystalline-rich particles (Fig. 1) having intermediate median ε_{Nd}, $^{87}Sr/^{86}Sr$ and smectite signatures such as those observed in MIS3/4 sediments (Fig. 2). Similar synoptic conditions during GPM as during IPM in autumn (Fig. 4d,f) and the reinforcement of autumn and winter precipitation over the coast points to sustained moisture advection by Mediterranean storm tracks and cyclogenesis at times of high obliquity and large NHIS during MIS3/4[8,34,36] (Fig. 3d,e).

Enrichments in volcanic-derived particles indicates pluvial episodes reaching as far south as volcanic fields in northern Libya (Fig. 1, 3b-c). Higher-frequency fluctuations between arid and humid phases during MIS3/4 are documented by the rapid alternation of coarser and finer sedimentation modes. Recurrent enrichments in coarser particles reflect arid inceptions that seem to occur preferentially during periods of North Atlantic climatic instabilities, such as Heinrich Events (HE)[6,9] (Fig. 3c,d).

We present here evidence for intermittent humid phases during MIS3 and MIS4 with winter precipitation probably reaching volcanic fields located around 28ºN (Fig. 4f). This climatic regime permitted the development of transient green corridors along the northern African coast, which repeatedly connected Morocco to the Levant[9].

A climatic context for human populations and migration

By providing a spatial and temporal framework for the reactivation of river systems in northern Africa, our record from the GS offers a unique window into the living conditions, habitats and potential dispersal corridors of prehistoric human populations[4,5]. We demonstrate that during warm interglacial periods, large river systems were flowing from the central Sahara to the Libyan coast for extended periods of time. Owing to a highly seasonal precipitation pattern, these rivers mostly flowed during summer and autumn, with the Sahabi and Kufrah rivers being likely perennial[19,30]. We further show that in addition to these green corridors, the entire area between 25ºN and the coast was probably vegetated and humid during these times, with highest precipitation from late summer to early spring (Fig. 4c,d and Extended data Fig. 5b). According to our proxy-record and model data, such conditions were maintained for about 5000 yrs, before switching back to arid conditions (Fig. 3b,c,e). During the glacial precipitation minima in our record, low precipitation was maintained along the Libyan coast but latitudes south of 30ºN were likely hyper-arid (Fig. 4e,f) and became areas of intense dust production. These drastic hydrological changes led to extensive shifts in vegetation and food resources in northern Africa, which likely played a crucial role for Pleistocene human population structure and evolution[37,38]. The combination of environmental changes and multi-millennial stability of humid climates provided windows for encounter and interaction of populations that probably exerted a strong evolutionary forcing and fostered technological innovations[39–41]. Associated landscape evolution may also have played a decisive role for the dispersal of populations across and beyond Africa[31].

During glacial MIS3 and MIS4, limited precipitation occurred over the Tibesti, which was not sufficient to trigger major river flow across Libya (Fig. 4e). Latitudes south of 28-30ºN were largely arid while the coastal zone received precipitation via Mediterranean storm tracks and local cyclogenesis during autumn and winter[12] (Fig. 4f and Extended data Fig.

5b). Rapid shifts between humid and arid conditions during MIS3/4 likely reflect the influence of northern Hemisphere climate instabilities on Saharan climates[9] (Fig. 3b,c). Sustained humidity along the coast may, however, have provided a refugium for human and animal populations, as previously suggested by continuous occupation of the Hauah Fteah cave in northern Libya[10,42]. While the existence and importance of migration corridors is presently being re-evaluated[43], our data suggest that the southern Mediterranean and northern African coast provided a favourable and relatively stable living habitat throughout the last glacial cycle, which may have allowed populations to move and mix[10,44,45].

References

1. Drake, N. A., Blench, R. M., Armitage, S. J., Bristow, C. S. & White, K. H. Ancient watercourses and biogeography of the Sahara explain the peopling of the desert. *Proc. Natl. Acad. Sci.* **108**, 458–462 (2011).
2. Lézine, A.-M., Hély, C., Grenier, C., Braconnot, P. & Krinner, G. Sahara and Sahel vulnerability to climate changes, lessons from Holocene hydrological data. *Quat. Sci. Rev.* **30**, 3001–3012 (2011).
3. Claussen, M., Dallmeyer, A. & Bader, J. *Theory and Modeling of the African Humid Period and the Green Sahara*. vol. 1 (Oxford University Press, 2017).
4. Hublin, J.-J. *et al.* New fossils from Jebel Irhoud, Morocco and the pan-African origin of *Homo sapiens*. *Nature* **546**, 289 (2017).
5. Scerri, E. M. L. The North African Middle Stone Age and its place in recent human evolution. *Evol. Anthropol. Issues News Rev.* **26**, 119–135 (2017).
6. Tjallingii, R. *et al.* Coherent high- and low-latitude control of the northwest African hydrological balance. *Nat. Geosci.* **1**, 670–675 (2008).

7. Larrasoaña, J. C., Roberts, A. P. & Rohling, E. J. Dynamics of Green Sahara Periods and Their Role in Hominin Evolution. *PLoS ONE* **8**, e76514 (2013).
8. Kutzbach, J. E. *et al.* African climate response to orbital and glacial forcing in 140,000-y simulation with implications for early modern human environments. *Proc. Natl. Acad. Sci.* 201917673 (2020) doi:10.1073/pnas.1917673117.
9. Ehrmann, W., Schmiedl, G., Beuscher, S. & Krüger, S. Intensity of African Humid Periods Estimated from Saharan Dust Fluxes. *PLOS ONE* **12**, e0170989 (2017).
10. Hoffmann, D. L. *et al.* Timing and causes of North African wet phases during the last glacial period and implications for modern human migration. *Sci. Rep.* **6**, (2016).
11. Abouelmagd, A. *et al.* Toward a better understanding of palaeoclimatic regimes that recharged the fossil aquifers in North Africa: Inferences from stable isotope and remote sensing data. *Palaeogeogr. Palaeoclimatol. Palaeoecol.* **329–330**, 137–149 (2012).
12. Rogerson, M. *et al.* Enhanced Mediterranean water cycle explains increased humidity during MIS 3 in North Africa. *Clim. Past* **15**, 1757–1769 (2019).
13. Tierney, J. E., Pausata, F. S. R. & deMenocal, P. B. Rainfall regimes of the Green Sahara. *Sci. Adv.* **3**, e1601503 (2017).
14. Paillou, P. *et al.* Mapping of a major paleodrainage system in eastern Libya using orbital imaging radar: The Kufrah River. *Earth Planet. Sci. Lett.* **277**, 327–333 (2009).
15. Skonieczny, C. *et al.* African humid periods triggered the reactivation of a large river system in Western Sahara. *Nat. Commun.* **6**, 8751 (2015).
16. Causse, C. *et al.* Humidity changes in southern Tunisia during the Late Pleistocene inferred from U–Th dating of mollusc shells. *Appl. Geochem.* **18**, 1691–1703 (2003).
17. Bout-Roumazeilles, V. *et al.* Tracking atmospheric and riverine terrigenous supplies variability during the last glacial and the Holocene in central Mediterranean. *Clim Past* **9**, 1065–1087 (2013).

18. Wu, J. *et al.* North-African paleodrainage discharges to the central Mediterranean during the last 18,000 years: A multiproxy characterization. *Quat. Sci. Rev.* **163**, 95–113 (2017).
19. Osborne, A. H. *et al.* A humid corridor across the Sahara for the migration of early modern humans out of Africa 120,000 years ago. *Proc. Natl. Acad. Sci.* **105**, 16444–16447 (2008).
20. Blanchet, C. L., Frank, M. & Schouten, S. Asynchronous Changes in Vegetation, Runoff and Erosion in the Nile River Watershed during the Holocene. *PLOS ONE* **9**, e115958 (2014).
21. Revel, M. *et al.* 100,000 Years of African monsoon variability recorded in sediments of the Nile margin. *Quat. Sci. Rev.* **29**, 1342–1362 (2010).
22. Beuscher, S. *et al.* End-member modelling as a tool for climate reconstruction—An Eastern Mediterranean case study. *PLOS ONE* **12**, e0185136 (2017).
23. Blanchet, C. L. A database of marine and terrestrial radiogenic Nd and Sr isotopes for tracing earth-surface processes. *Earth Syst. Sci. Data* **11**, 741–759 (2019).
24. Schepanski K. *et al.* Meteorological processes forcing Saharan dust emission inferred from MSG-SEVIRI observations of subdaily dust source activation and numerical models. *J. Geophys. Res. Atmospheres* **114**, (2009).
25. Weltje, G. J. End-member modeling of compositional data: Numerical-statistical algorithms for solving the explicit mixing problem. *Math. Geol.* **29**, 503–549 (1997).
26. O'Hara, S. L., Clarke, M. L. & Elatrash, M. S. Field measurements of desert dust deposition in Libya. *Atmos. Environ.* **40**, 3881–3897 (2006).
27. Goudie, A. S. & Middleton, N. J. Saharan dust storms: nature and consequences. *Earth-Sci. Rev.* **56**, 179–204 (2001).
28. Peyron, O. *et al.* Quantitative reconstructions of annual rainfall in Africa 6000 years ago: Model-data comparison. *J. Geophys. Res. Atmospheres* **111**, (2006).

29. Bartlein, P. J. *et al.* Pollen-based continental climate reconstructions at 6 and 21 ka: a global synthesis. *Clim. Dyn.* **37**, 775–802 (2011).

30. Coulthard, T. J., Ramirez, J. A., Barton, N., Rogerson, M. & Brücher, T. Were Rivers Flowing across the Sahara During the Last Interglacial? Implications for Human Migration through Africa. *PLoS ONE* **8**, e74834 (2013).

31. Timmermann, A. & Friedrich, T. Late Pleistocene climate drivers of early human migration. *Nature* **538**, 92–95 (2016).

32. Wagner, B. *et al.* Mediterranean winter rainfall in phase with African monsoons during the past 1.36 million years. *Nature* (2019) doi:10.1038/s41586-019-1529-0.

33. Kutzbach, J. E., Chen, G., Cheng, H., Edwards, R. L. & Liu, Z. Potential role of winter rainfall in explaining increased moisture in the Mediterranean and Middle East during periods of maximum orbitally-forced insolation seasonality. *Clim. Dyn.* **42**, 1079–1095 (2014).

34. Bosmans, J. H. C. *et al.* Precession and obliquity forcing of the freshwater budget over the Mediterranean. *Quat. Sci. Rev.* **123**, 16–30 (2015).

35. Rohling, E. J., Marino, G. & Grant, K. M. Mediterranean climate and oceanography, and the periodic development of anoxic events (sapropels). *Earth-Sci. Rev.* **143**, 62–97 (2015).

36. Davis, B. A. S. & Brewer, S. Orbital forcing and role of the latitudinal insolation/temperature gradient. *Clim. Dyn.* **32**, 143–165 (2009).

37. Scerri, E. M. L., Drake, N. A., Jennings, R. & Groucutt, H. S. Earliest evidence for the structure of Homo sapiens populations in Africa. *Quat. Sci. Rev.* **101**, 207–216 (2014).

38. Gunz, P. *et al.* Early modern human diversity suggests subdivided population structure and a complex out-of-Africa scenario. *Proc. Natl. Acad. Sci.* pnas.0808160106 (2009) doi:10.1073/pnas.0808160106.

39. Scerri, E. M. L. *et al.* Did Our Species Evolve in Subdivided Populations across Africa, and Why Does It Matter? *Trends Ecol. Evol.* **33**, 582–594 (2018).

40. Mcbrearty, S. & Brooks, A. S. The revolution that wasn't: a new interpretation of the origin of modern human behavior. *J. Hum. Evol.* **39**, 453–563 (2000).

41. Ziegler, M. *et al.* Development of Middle Stone Age innovation linked to rapid climate change. *Nat. Commun.* **4**, 1905 (2013).

42. Jacobs, Z. *et al.* The chronostratigraphy of the Haua Fteah cave (Cyrenaica, northeast Libya) — Optical dating of early human occupation during Marine Isotope Stages 4, 5 and 6. *J. Hum. Evol.* **105**, 69–88 (2017).

43. Groucutt Huw S. *et al.* Rethinking the dispersal of Homo sapiens out of Africa. *Evol. Anthropol. Issues News Rev.* **24**, 149–164 (2015).

44. Secher, B. *et al.* The history of the North African mitochondrial DNA haplogroup U6 gene flow into the African, Eurasian and American continents. *BMC Evol. Biol.* **14**, 109 (2014).

45. Sankararaman, S., Patterson, N., Li, H., Pääbo, S. & Reich, D. The Date of Interbreeding between Neandertals and Modern Humans. *PLOS Genet.* **8**, e1002947 (2012).

46. Drake, N. A. *et al.* Reconstructing palaeoclimate and hydrological fluctuations in the Fezzan Basin (southern Libya) since 130 ka: A catchment-based approach. *Quat. Sci. Rev.* **200**, 376–394 (2018).

47. Harris, I., Jones, P. D., Osborn, T. J. & Lister, D. H. Updated high-resolution grids of monthly climatic observations - the CRU TS3.10 Dataset. *Int. J. Climatol.* **34**, 623–642 (2014).

48. Laskar, J. *et al.* A long-term numerical solution for the insolation quantities of the Earth. *Astron. Astrophys.* **428**, 261–285 (2004).

Corresponding author

Correspondence and requests for materials should be addressed to Cécile Blanchet (blanchet@gfz-potsdam.de)

Acknowledgements

We thank the captain, crew and scientific team of R.V. PELAGIA cruise 64PE349 as well as Piet van Gaever and Rineke Gieles (in memoriam) at NIOZ for analytical assistance. CLB acknowledges the support of GFZ Potsdam through a reintegration grant. RT acknowledges financial support by NWO grants INTAX (839.08.434) and SCAN2. WE was supported by a grant from the Deutsche Forschungsgemeinschaft (EH89/19-1). AT was supported by the Institute for Basic Science (IBS) IBS-R028-D1.

Author contributions

CLB, AHO and RT conceived the study and organised cruise 64PE349, led by WB. WB and AHO retrieved the sediment cores. AHO and MF facilitated and measured the radiogenic isotopes; RT measured the grain-size distributions, oxygen isotopes and XRF core scanning; WE measured the clay mineral assemblages; TF and AT developed and ran the LOVECLIM simulations. CLB analysed the data and wrote the manuscript with input from all co-authors. AT, WB and MF provided logistical and financial support.

Competing interests

The other authors declare no competing interests.

Figure captions

Fig. 1: Map of northern Africa with records relevant for our study. Location of core 64PE349-8 and other marine records MD04-2797[17], CP10BC[18], SL71[9,22] and ODP971A[19]. Terrestrial sites: (1) Chott-El-Jerid[16], (2) Haua Fteah[42] and Susah cave[10,12] and (3) palaeo-

399 lake Fezzan[46]. Palaeo-river systems and wadis redrawn from ref.[1]. Libyan volcanic fields:
400 (G) Guaryan, (AS) As-Sawda, (AH) Al Haruj, (WaN) Waw-An-Namus, (JN) Jebel Nuqay
401 and (IE) In Ezzane. ε_{Nd} of rocks and surface sediments from ref.[23] and present-day winter
402 precipitation rates from ref.[47]. Map background represents the topography, bathymetry and
403 political borders (Gebco 2014 30-arc second grid, www.gebco.net).

404 **Fig. 2: Tracers of past fluvial input into the Gulf of Sirte.** a: Scatter plot of $^{87}Sr/^{86}Sr$ vs.
405 ε_{Nd} in detrital sediments from core 64PE349-8. All regional isotopic signatures derive from
406 ref.[23] (Extended data Tables 2 and 3), surface sediments for PDS[24] (preferential dust
407 sources, Extended data Fig. 1) as box and whisker plots (median and quartiles, see
408 Methods); sapropel layers, glacial MIS3/4 and non-sapropel sediments as median values.
409 Sediments from core 64PE349-8 fall within an array defined by three end-members: EM
410 Palaeo-rivers: gastropods from palaeo-river channel beds[19]; EM Libyan sediments:
411 gastropods from Libyan soils[19] and PDS2-3; EM Dust: PDS1, PDS4-6. b-e: Box and
412 whisker plots for ε_{Nd} values (b), $^{87}Sr/^{86}Sr$ ratio (c), log-ratio of
413 smectite/(kaolinite+palygorskite) (d) and log-ratio of grain-size end-members EM1/EM3
414 (e).

415 **Fig. 3: Hydroclimate records of core 64PE349-8 compared to transient simulations**
416 **of precipitation**. a-c: Gulf of Sirte (64PE349-8). a: $\delta^{18}O$ in *G. ruber;* b: ε_{Nd} of the detrital
417 fraction (purple, with 2σ uncertainty) and log-ratio of smectite/(kaolinite+palygorskite)
418 (brown); c: $^{87}Sr/^{86}Sr$ (black, with 2σ uncertainty) and proportions of grain-size end-
419 members EM1 (green), EM2 (yellow) and EM3 (light grey). d-e: Regional records and
420 forcing. d: Humidity index from core GeoB7920 offshore Senegal[6] (red); $\delta^{18}O$ in Susah
421 Cave speleothem (N Libya)[10] (black, moving average); obliquity of the Earth's axis (dashed
422 curve) and precession parameter (brown)[48]. Heinrich events are labelled as H1-H6 and
423 C19-C24[6]. e: LOVECLIM simulation of MAP in coastal Libya (red) and over Tibesti

latitudes (green) (see Fig. 4 for spatial averaging). Bottom bar: interglacial (black) and glacial (white) marine isotope stages.

Figure 4. Summer and autumn precipitation as modelled by LOVECLIM during interglacial and glacial precession minima. a and b: MAP during the past 160 ka over the Tibesti latitudes (a) and coastal Libya (b), with interglacial precession minima (IPM, red) and glacial precession minima (GPM, blue) (see Extended data Fig. 4 for IPM and GPM definition). c and d: IPM intervals. Summer (JJA) (c) and Autumn (SON) (d) precipitation and wind fields for northern Africa with boxes indicating spatial averaging of simulated precipitation (orange) for the Tibesti latitudes (c) and coastal Libyan latitudes (d). e and f: same as c and d for GPM intervals.

Methods

Core description and age model

Core 64PE349-8 was retrieved from the Gulf of Sirte during R.V. Pelagia cruise 64PE349 in December 2011 and reached a total length of 10.32 m (Extended data Fig. 1, 2). The upper 5 m of the sediment core presented here are composed of hemipelagic clays and silty-clays that show traces of bioturbation. A well-sorted layer with a coarse base and fining-upward sequence indicates a 25 cm-thick turbidite between 349 and 324 cm core depth (where sampling was avoided). The sedimentary sequence of core 64PE349-8 exhibits four layers characterized by a typical sapropel facies consisting of dark-coloured well preserved sapropels and underlying greyish-coloured proto-sapropels (Extended data Fig. 2a). In addition to the visual identification, we used magnetic susceptibility[49] and barium/aluminium (Ba/Al) ratios[50] (Extended data Fig. 2c,d and Source data) to detect the

447 original extent of the sapropels given that parts of these deposits may have been
448 reoxidized.
449 The age model for core 64PE349-8 was constructed by integrating a set of 5 Accelerator
450 Mass Spectrometer (AMS) radiocarbon ages, a tephra layer and tie-points obtained by
451 tuning the $\delta^{18}O$ signal of planktonic foraminifera (*Globigerinoides ruber*) to regional and
452 reference $\delta^{18}O$ records (Extended data Fig. 2a and Source data). The AMS dating was
453 performed at the Leibniz-Laboratory (Kiel, Germany) and covers the uppermost 90 cm of
454 core 64PE349-8 (Source data). The radiocarbon ages were calibrated with the Marine13
455 calibration curve[51] and a standard marine reservoir age of 400 yrs using the Oxcal online
456 software[52]. Three tephra layers were identified by their chemical signature (e.g., magnetic
457 susceptibility or elemental ratios) at 134, 223 and 382 cm (Extended data Fig. 2). Only the
458 well-identified Campanian Ignimbrite Y-5 tephra at 134 cm was used for the age model
459 and provided a tie-point at 39.28 ka BP[53]. Additional tie-points were obtained by correlating
460 the planktic $\delta^{18}O$ record of core 64PE349-8 to several reference records: 1) the U/Th-
461 dated speleothem of Soreq Cave[54], 2) core LC21 from the Aegean basin[54], 3) the nearby
462 core KC01B (dated by tephrochronology and orbital tuning)[55] and 4) the LR04 benthic
463 $\delta^{18}O$ stack[56]. An outlier analysis as well as estimation of most probable ages for each tie-
464 point and associated uncertainty was realised using the Bayesian analysis of the Oxcal
465 software[52,57].
466 According to our age model, the upper 4 m of core 64PE349-8 cover the past 160 ka. The
467 calculated sedimentation rates range from 1 to 12 cm/ka (Extended data Fig. 2b) They
468 decrease gradually downcore, which may reflect an artificial elongation of the upper part of
469 the core during coring. Specific intervals of high sedimentation rates include sapropel S1
470 and the last glacial maximum but most sapropel layers are actually characterized by
471 decreases of the sedimentation rate.

Stable oxygen and carbon isotopes

The stable isotope ratios of oxygen ($\delta^{18}O$) and carbon ($\delta^{13}C$) were measured on ~10 shells (~20 mg) of planktonic foraminifera *Globigerinoides ruber* (white) (Source data). The foraminifera were retrieved from sieved sediment samples taken at 5-cm resolution. The measurements were made on a Thermo-MAT253 mass spectrometer in the department "Ocean Systems" at the NIOZ and were calibrated against the Pee-Dee Belemnite (PDB). Drift corrections and assessment of the accuracy and precision of the measurements were obtained by repeated (every 10^{th} sample) measurements of the international standard NBS-19 and an internal standard (VICS).

Radiogenic neodymium and strontium isotopes

The radiogenic isotope composition of neodymium (Nd) and strontium (Sr) was measured on the siliciclastic fraction of the sediments (Source data). Dry sediment samples of approximately 0.05 g were decarbonated and leached (using sequential acetic acid and hydroxylamine hydrochloride treatments) prior to being totally dissolved using concentrated hydrochloric, nitric and hydrofluoric acids. Standard column-chromatography procedures were applied to separate and purify Nd and Sr[58–60]. The Nd and Sr isotope compositions were measured on a Nu Instruments multi-collector inductively-coupled plasma mass spectrometer (MC-ICP-MS) at GEOMAR. Blank levels were negligible for both radiogenic Nd and Sr isotopes (<0.04 ng or < 0.02% of sample size for Nd and <0.63 ng or < 1.4% of sample size for Sr). The isotope results were normalized to the accepted values of the JNdi standard for Nd ($^{143}Nd/^{144}Nd=0.512115$)[61] and of the NIST SRM 987 standard for Sr ($^{86}Sr/^{87}Sr=0.710245$). The Nd isotope ratios are reported as ε_{Nd}, which is the $^{143}Nd/^{144}Nd$ ratio normalized to CHUR ($^{143}Nd/^{144}Nd=0.512638$[62]) and multiplied by 10,000. External reproducibility was estimated by repeated measurements of the in-house SPC and SPEX standards, as well as the JNdi standard for Nd, and an AA standard as

497 well as the NIST SRM 987 standard for Sr. The standard 2σ uncertainty for each
498 measurement session is reported and was ≤ 0.5 ε_{Nd} units for Nd and <±0.000028 for Sr.

499 **Grain-size distribution and end-member modelling**

500 The siliciclastic fraction of the sediments was separated from the bulk sediment samples
501 by removing carbonates using a 1M hydrochloride acid solution and subsequently
502 dissolving organic matter using concentrated hydrogen peroxide following Tjallingii et al.[6].
503 In order to prevent the neoformation of particle aggregates, the residual samples were
504 shortly boiled with a sodium pyrophosphate solution before measuring the grain-size
505 distribution using a Coulter Laser Seizer (LS230) at the NIOZ (The Netherlands).
506 Statistically meaningful end-members (EMs) were calculated from the total set of grain-
507 size measurements (n=86) using the end-member model algorithm EMMA[25] (Extended
508 data Fig. 3). In this case, a three-EM model explains 97.4% of the total amount of
509 variance, with an average coefficient of determination of 0.68 having lower values (0.35)
510 around 40µm (Extended data Fig. 3 and Source data). The changes in proportion of the
511 EMs were explored using centred log-ratios in order to avoid the constant-sum
512 constraint[63]. This log-ratio transformation allows meaningful comparison mean and median
513 values of populations that would otherwise have non-normal distributions and be
514 intrinsically correlated.

515 **Clay Mineralogy**

516 Freeze-dried bulk sediment samples were treated with 3% hydrogen peroxide and 10%
517 acetic acid in order to remove organic and calcareous components. The clay (<2 µm) was
518 separated from the coarse fraction in settling tubes following the Atterberg method. Then,
519 40 mg of clay suspension were mounted as texturally oriented aggregates by rapidly
520 filtering the suspension through a membrane filter with 0.15 µm pore width. The filter cakes

were dried at 60°C and mounted on aluminium tiles. The samples were exposed to ethylene-glycol vapour at a temperature of 60°C for at least 18 hours immediately before the measurements. XRD analyses were conducted on a diffractometer system Rigaku Miniflex with CoKα radiation (30 kV, 15 mA) in the range 3-40°2Θ (step size 0.02°2Θ, measuring time 2 sec/step). The range 27.5-30.6°2Θ was measured at a higher resolution (step size 0.01°2Θ, measuring time 4 sec/step) in order to better resolve the (002) peak of kaolinite and the (004) peak of chlorite. The X-ray diffractograms were evaluated using the interactive "MacDiff" software[64]. The main clay minerals were identified by their basal reflections at 17 Å (smectite; glycolated), 10 and 5 Å (illite), 14.2, 7, 4.72 and 3.54 Å (chlorite), 7 and 3.58 Å (kaolinite) and 10.5 Å (palygorskite). Semi-quantitative evaluations of the clay mineral assemblages were performed on the integrated peak areas, using empirically estimated and well-established weighting factors[65,66]. Changes in the proportion of clay minerals between sedimentary populations and downcore were explored using centred log ratios in order to avoid limitations associated with the constant-sum constraint (see previous section) (Source data).

Transient modelling using LOVECLIM

The Earth system model LOVECLIM was used to conduct transient simulations of the last 784,000 years. LOVECLIM is a coupled ocean–atmosphere–sea-ice–vegetation model[67]. The atmospheric component of LOVECLIM is the spectral T21, three-level model ECBilt[68], which is based on quasi-geostrophic equations that are extended by estimates of geostrophic terms. The ocean–sea-ice component of LOVECLIM consists of a free-surface Ocean General Circulation Model with a 3° x 3° horizontal resolution coupled to a dynamic–thermodynamic sea-ice model[69]. Atmosphere and ocean components are coupled through the exchange of freshwater and heat fluxes. The vegetation component

545 VECODE of the model computes the evolution of terrestrial vegetation cover based on
546 annual mean surface temperature and precipitation[70].
547 The transient simulations were forced by time-dependent boundary conditions for orbital
548 parameters[71], atmospheric green-house gas (GHG) concentrations, Northern Hemisphere
549 ice sheet (NHIS) orography and albedo[72] following the previously published
550 methodology[73]. Atmospheric GHG concentrations were prescribed according to
551 reconstructions from EPICA Dome C for carbon dioxide[74] as well as methane and nitrous
552 oxide[75]. Orbital forcing and atmospheric GHG concentrations were updated every model
553 year. The effects of NHIS on albedo and land topography were prescribed according to a
554 previously published study[73]. The forcing was applied with an acceleration factor of 5,
555 which compresses 784,000 forcing years into 156,000 model years. This acceleration
556 factor is appropriate for quickly equilibrating surface variables. The model simulation is an
557 updated version of the one presented in a previous study[76] and uses a higher climate
558 sensitivity, resulting in a better representation of the glacial–interglacial surface
559 temperature amplitude[31]. It must be noted that millennial-scale variability such as Heinrich
560 events is not accounted for in the transient simulations due to the lack of robust freshwater
561 forcing reconstructions and the use of accelerated forcing. Some discrepancies can be
562 identified when comparing to present-day precipitation dynamics (Extended data Fig. 5a).
563 Late summer and early autumn precipitation are overestimated over the Libyan coast while
564 the winter precipitation is underestimated. However, the moisture advection through
565 Mediterranean storm tracks and cyclogenesis is well captured by LOVECLIM and is very
566 similar to the climatic dynamics described in Wagner et al.[32]. The seasonal northward
567 displacement of the ITCZ is well represented in LOVECLIM (Extended data Fig. 5a). The
568 resolution of the atmospheric model component, however, results in a larger meridional
569 extent of the simulated ITCZ and the strong meridional rainfall gradient across the Tibesti
570 region cannot be fully captured. Also, the AMOC is very strong in LOVECLIM leading to a

571 warm bias in the Northern Hemisphere. The latter might pull the ITCZ further north during
572 pre-industrial conditions. In addition, the low resolution of the atmospheric model cannot
573 resolve some of the topographic details.
574 The results of four sensitivity simulations with respect to rainfall dynamics in both regions
575 are shown in Extended data Fig. 6. The sensitivity simulations cover 408,000 years and
576 were designed and conducted to explore the individual effects of atmospheric GHGs,
577 NHIS and orbital parameters on climate dynamics. Two simulations were designed to
578 study the role of orbital forcing under warm and cold climate respectively (Extended data
579 Fig. 6a,b,e,f). For both simulations, transient orbital parameters are used. However, one
580 simulation was run under constant preindustrial atmospheric CO_2 concentration of 280
581 ppm, whereas the second simulation uses a constant atmospheric CO2 concentration of
582 200 ppm, resulting in a colder background climate. The third sensitivity simulation uses
583 transient forcing as described above but constant preindustrial NHIS (extent and albedo)
584 (Extended data Fig. 6c,g). The 'NHIS effect' is calculated as the difference between the
585 full-forcing simulation and this simulation (green shaded area in Extended data Fig. 6c,g).
586 The last sensitivity simulation uses transient forcing as described above but constant
587 preindustrial atmospheric GHG concentrations (Extended data Fig. 6d,h). The 'GHG effect'
588 can then be calculated as the difference between the simulation using the full forcing and
589 this simulation (pink shaded area in Extended data Fig. 6d,h).

590 **Data analyses and plotting**

591 Geochemical and sedimentological data were analysed using the freeware R[77], which was
592 also used to create the maps in Fig. 1 and Extended data Fig. 1 (with package
593 "marmap"[78]) and the box and whisker plots in Fig. 2b-e (with package "ggplot2"[79]).
594 Data points were analysed as part of populations characterised by their temporal range or
595 lithology. Sapropel layers were defined based on their lithology (see section "Core

description" and Extended data Fig. 2): S1 = 13-37 cm, S3 = 236-243 cm, S4 = 281-296 cm and S5 = 337-377 cm. The glacial MIS3/4 interval has been defined as covering the interval 34.25-68.8 ka and corresponds to depth interval 120-210 cm (Extended data Fig. 2). All other samples constitute the non-sapropel (NS) population.

Since the sample number n was higher than five for all populations, box plots were used to compare their means and medians (Fig. 2b-e)[80]. Box plots allow to visualise the relationship between mean (blue dots) and median (black line), as well as the interquartile range (IQ, shown as boxes) (i.e., between 25% and 75% quantiles) for each population. Samples falling out of a 1.5*IQ interval are considered as outliers (here depicted as red diamonds). The 95% confidence intervals around the mean (CI = 1.58*IQ/$\sqrt{n}$) were calculated in order to evaluate the significance of the observed variability (dashed lines).

Data availability

All datasets presented here will be made freely available at the data repository PANGAEA (https://pangaea.de/) and are provided as source data for Fig. 1, 2, 3 and Extended Data Fig. 1, 2. Transient LOVECLIM simulations are available at: https://climatedata.ibs.re.kr/grav/data/loveclim-784k.

Methods references

49. Larrasoaña, J. C., Roberts, A. P. & Rohling, E. J. Magnetic susceptibility of eastern Mediterranean marine sediments as a proxy for Saharan dust supply? *Mar. Geol.* **254**, 224–229 (2008).

50. De Lange, G. J. *et al.* Synchronous basin-wide formation and redox-controlled preservation of a Mediterranean sapropel. *Nat. Geosci.* **1**, 606–610 (2008).

619 51. Reimer, P. J. *et al.* IntCal13 and Marine13 Radiocarbon Age Calibration Curves 0–
620 50,000 Years cal BP. *Radiocarbon* **55**, 1869–1887 (2013).
621 52. Bronk-Ramsey, C. Bayesian Analysis of Radiocarbon Dates. *Radiocarbon* **51**, 337–
622 360 (2009).
623 53. De Vivo, B. *et al.* New constraints on the pyroclastic eruptive history of the
624 Campanian volcanic Plain (Italy). *Mineral. Petrol.* **73**, 47–65 (2001).
625 54. Grant, K. M. *et al.* The timing of Mediterranean sapropel deposition relative to
626 insolation, sea-level and African monsoon changes. *Quat. Sci. Rev.* **140**, 125–141
627 (2016).
628 55. Lourens, L. J. Revised tuning of Ocean Drilling Program Site 964 and KC01B
629 (Mediterranean) and implications for the $\delta^{18}O$, tephra, calcareous nannofossil, and
630 geomagnetic reversal chronologies of the past 1.1 Myr. *Paleoceanography* **19**, n/a-n/a
631 (2004).
632 56. Lisiecki, L. E. & Raymo, M. E. A Pliocene-Pleistocene stack of 57 globally
633 distributed benthic $\delta^{18}O$ records. *Paleoceanography* **20**, n/a-n/a (2005).
634 57. Bronk Ramsey, C. Dealing with Outliers and Offsets in Radiocarbon Dating.
635 *Radiocarbon* **51**, 1023–1045 (2009).
636 58. Barrat, J. A. *et al.* Determination of Rare Earth Elements in Sixteen Silicate
637 Reference Samples by ICP-MS After Tm Addition and Ion Exchange Separation.
638 *Geostand. Newsl.* **20**, 133–139 (1996).
639 59. Horwitz, P. E., Chiarizia, R. & Dietz, M. L. A Novel Strontium Selective Extraction
640 Chromatographic Resin. *Solvent Extr. Ion Exch.* **10**, 313–336 (1992).
641 60. Le Fèvre, B. & Pin, C. A straightforward separation scheme for concomitant Lu–Hf
642 and Sm–Nd isotope ratio and isotope dilution analysis. *Anal. Chim. Acta* **543**, 209–221
643 (2005).

61. Tanaka, T. *et al.* JNdi-1: a neodymium isotopic reference in consistency with LaJolla neodymium. *Chem. Geol.* **168**, 279–281 (2000).

62. Jacobsen, S. B. & Wasserburg, G. J. Sm-Nd isotopic evolution of chondrites. *Earth Planet. Sci. Lett.* **50**, 139–155 (1980).

63. Kucera, M. & Malmgren, B. A. Logratio transformation of compositional data: a resolution of the constant sum constraint. *Mar. Micropaleontol.* **34**, 117–120 (1998).

64. Petschick, R. *MacDiff 4.2.6 (http://www.geol-pal.uni-frankfurt.de/Staff/Homepages/Petschick/MacDiff/MacDiffInfoE.html)*. (2001).

65. Biscaye, P. E. Mineralogy and Sedimentation of Recent Deep-Sea Clay in the Atlantic Ocean and Adjacent Seas and Oceans. *GSA Bull.* **76**, 803–832 (1965).

66. Weaver, C. E. & Beck, K. C. Miocene of the S.E. United States: A model for chemical sedimentation in a peri-marine environment. *Sediment. Geol.* **17**, IX–234 (1977).

67. Goosse, H. *et al.* Description of the Earth system model of intermediate complexity LOVECLIM version 1.2. *Geosci. Model Dev.* **3**, 603–633 (2010).

68. Opsteegh, J. D., Haarsma, R. J., Selten, F. M. & Kattenberg, A. ECBILT: a dynamic alternative to mixed boundary conditions in ocean models. *Tellus A* **50**, 348–367 (1998).

69. Goosse, H. & Fichefet, T. Importance of ice-ocean interactions for the global ocean circulation: A model study. *J. Geophys. Res. Oceans* **104**, 23337–23355 (1999).

70. Brovkin, V., Ganopolski, A. & Svirezhev, Y. A continuous climate-vegetation classification for use in climate-biosphere studies. *Ecol. Model.* **101**, 251–261 (1997).

71. Berger, A. Long-Term Variations of Daily Insolation and Quaternary Climatic Changes. *J. Atmospheric Sci.* **35**, 2362–2367 (1978).

72. Ganopolski, A. & Calov, R. The role of orbital forcing, carbon dioxide and regolith in 100 kyr glacial cycles. *Clim. Past* **7**, 1415–1425 (2011).

669 73. Timmermann, A. *et al.* Modeling Obliquity and CO_2 Effects on Southern
670 Hemisphere Climate during the Past 408 ka. *J. Clim.* **27**, 1863–1875 (2014).
671 74. Lüthi, D. *et al.* High-resolution carbon dioxide concentration record 650,000–
672 800,000 years before present. *Nature* **453**, 379–382 (2008).
673 75. EPICA community members. Eight glacial cycles from an Antarctic ice core. *Nature*
674 **429**, 623–628 (2004).
675 76. Friedrich, T., Timmermann, A., Tigchelaar, M., Timm, O. E. & Ganopolski, A.
676 Nonlinear climate sensitivity and its implications for future greenhouse warming. *Sci.*
677 *Adv.* **2**, e1501923 (2016).
678 77. R Core Team. *R: A language and environment for statistical computing*. (R
679 Foundation for Statistical Computing, 2013).
680 78. Pante, E. & Simon-Bouhet, B. marmap: A Package for Importing, Plotting and
681 Analyzing Bathymetric and Topographic Data in R. *PLOS ONE* **8**, e73051 (2013).
682 79. Wickham, H. *ggplot2: Elegant Graphics for Data Analysis.* (Springer-Verlag New
683 York, 2016).
684 80. Krzywinski, M. & Altman, N. Points of Significance: Visualizing samples with box
685 plots. *Nat. Methods* **11**, 119–120 (2014).

FIGURE 1

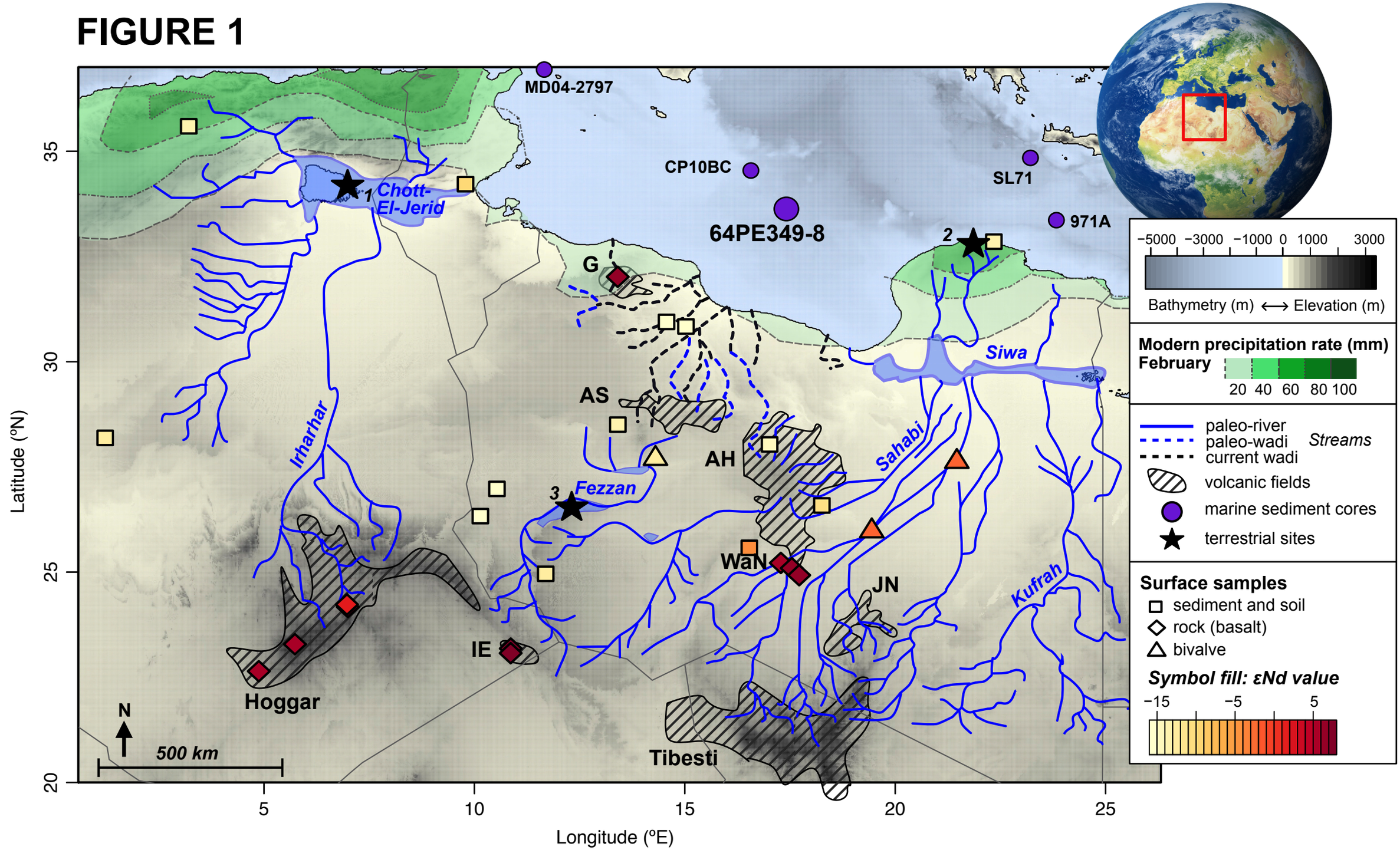
MD04-2797
CP10BC
SL71
64PE349-8
971A
1
Chott-El-Jerid
2
G
Siwa
AS
AH
Irharhar
Sahabi
3
Fezzan
WaN
JN
Kufrah
IE
Hoggar
Tibesti
N
500 km
Latitude (°N)
Longitude (°E)
20
25
30
35
5
10
15
20
25
−5000 −3000 −1000 0 1000 3000
Bathymetry (m) ⟷ Elevation (m)
Modern precipitation rate (mm)
February
20 40 60 80 100
paleo-river
paleo-wadi
current wadi
Streams
volcanic fields
marine sediment cores
terrestrial sites
Surface samples
sediment and soil
rock (basalt)
bivalve
Symbol fill: εNd value
−15 −5 5

FIGURE 2

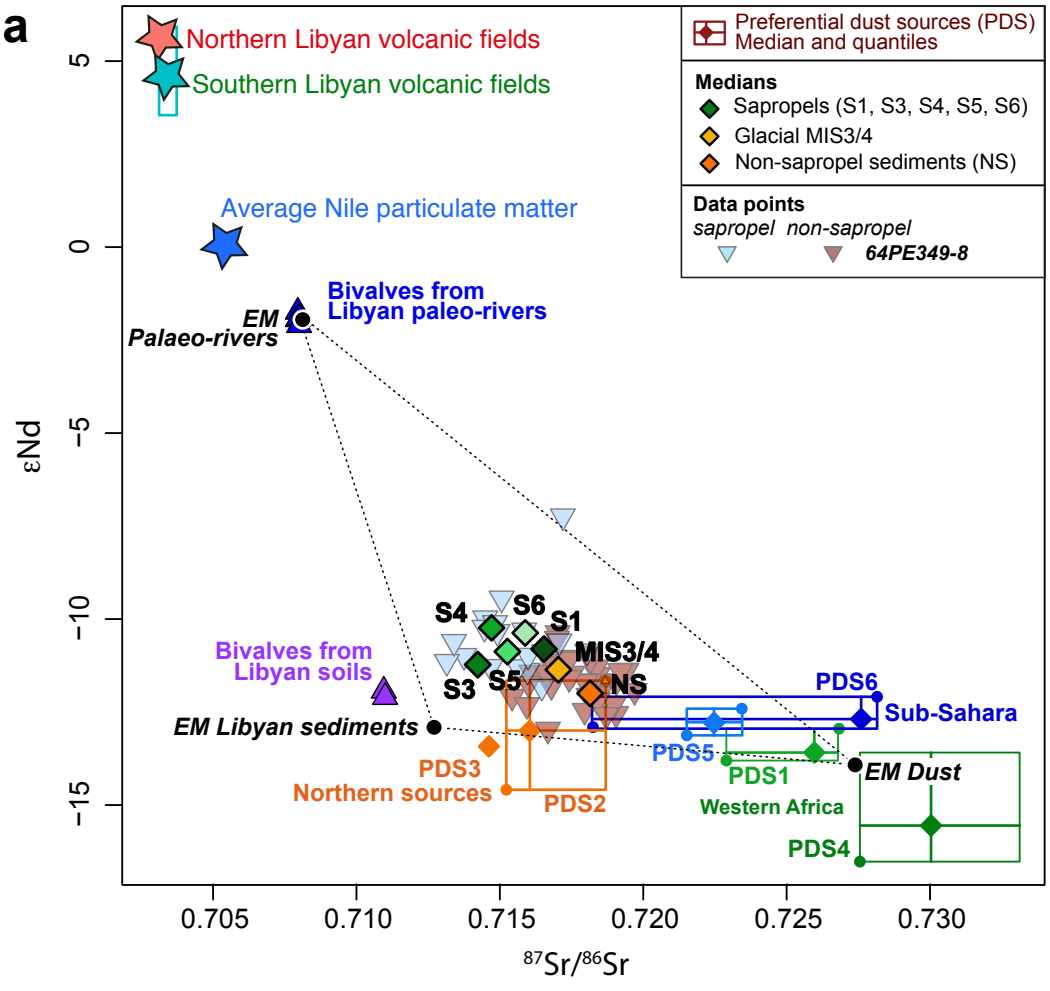
a
Northern Libyan volcanic fields
Southern Libyan volcanic fields
Average Nile particulate matter
EM Palaeo-rivers
Bivalves from Libyan paleo-rivers
Bivalves from Libyan soils
EM Libyan sediments
Northern sources
PDS3
PDS2
PDS1
Western Africa
PDS4
PDS5
PDS6
Sub-Sahara
EM Dust
S4
S6
S1
MIS3/4
S3
S5
NS
Preferential dust sources (PDS)
Median and quantiles
Medians
Sapropels (S1, S3, S4, S5, S6)
Glacial MIS3/4
Non-sapropel sediments (NS)
Data points
sapropel non-sapropel
64PE349-8
εNd
87Sr/86Sr
5
0
−5
−10
−15
0.705
0.710
0.715
0.720
0.725
0.730

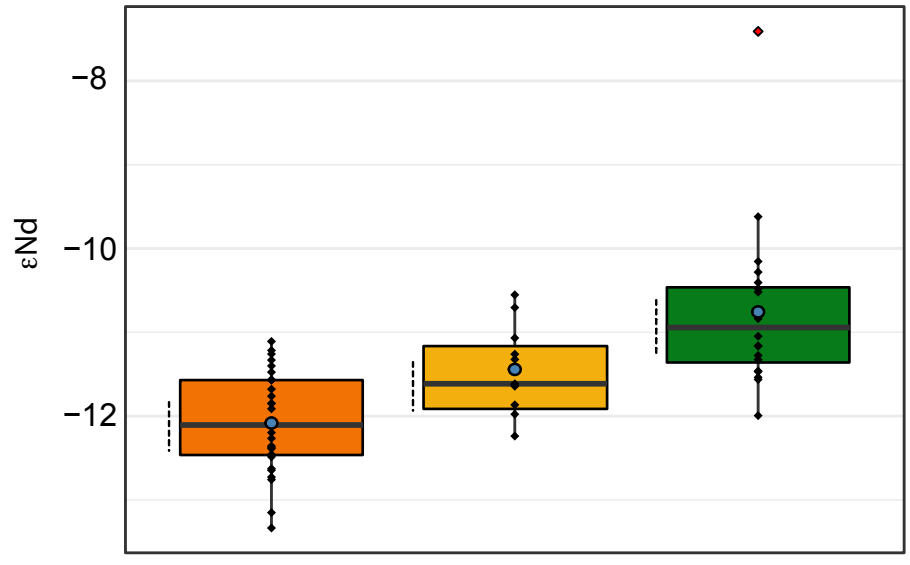
b.εNd
εNd
−8
−10
−12

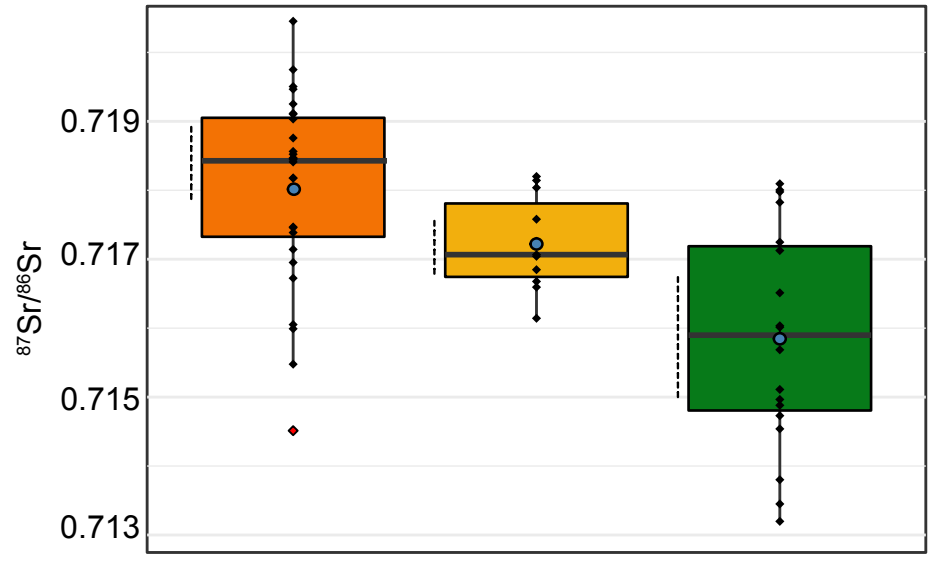
c.87Sr/86Sr
87Sr/86Sr
0.719
0.717
0.715
0.713

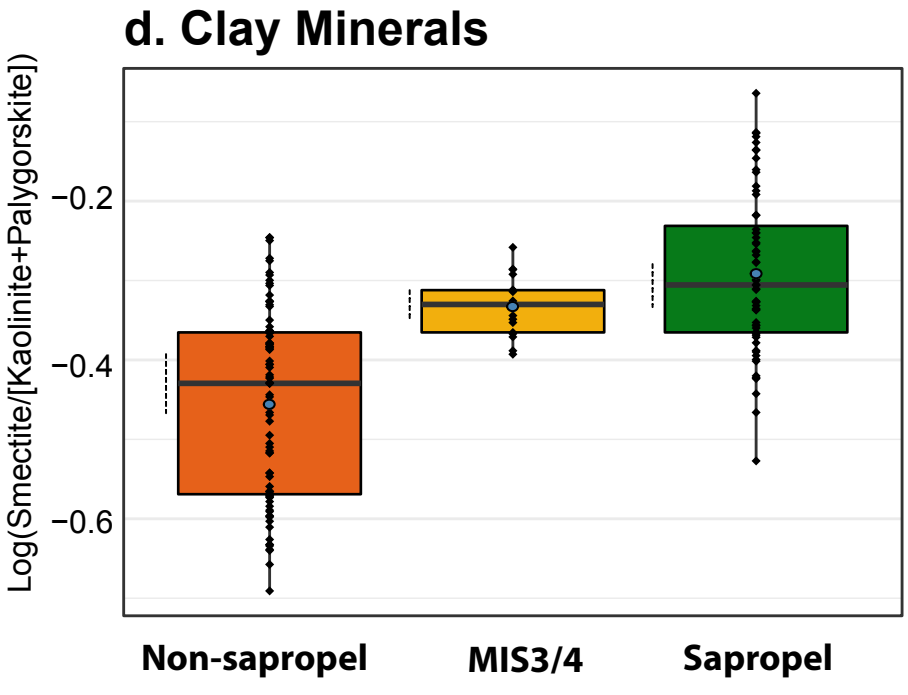
d. Clay Minerals
Log(Smectite/[Kaolinite+Palygorskite])
−0.2
−0.4
−0.6
Non-sapropel
MIS3/4
Sapropel

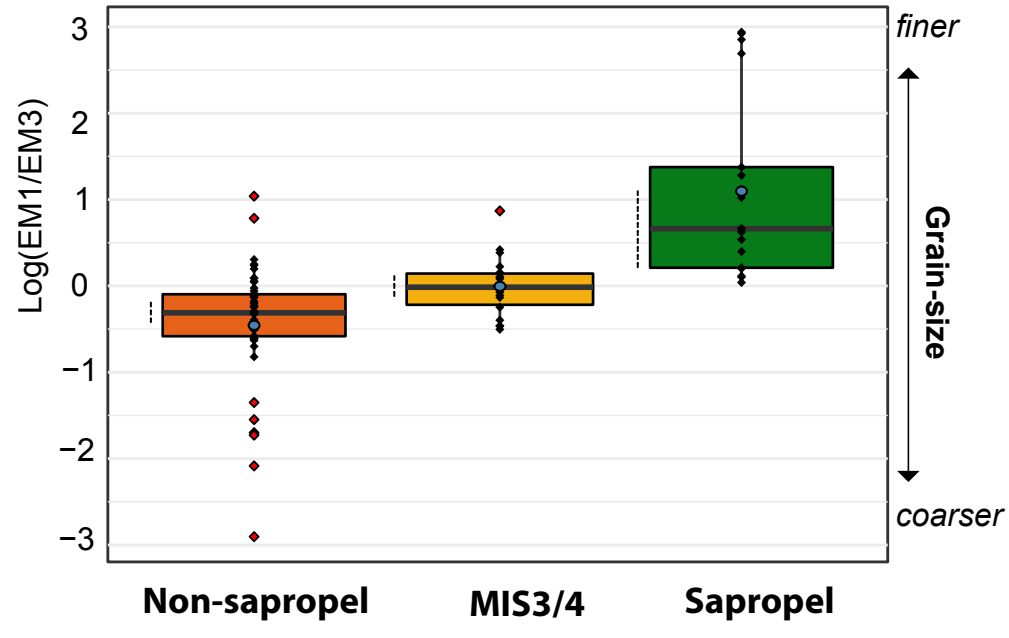
e. Grain size
Log(EM1/EM3)
3
2
1
0
−1
−2
−3
finer
Grain-size
coarser
Non-sapropel
MIS3/4
Sapropel

FIGURE 3

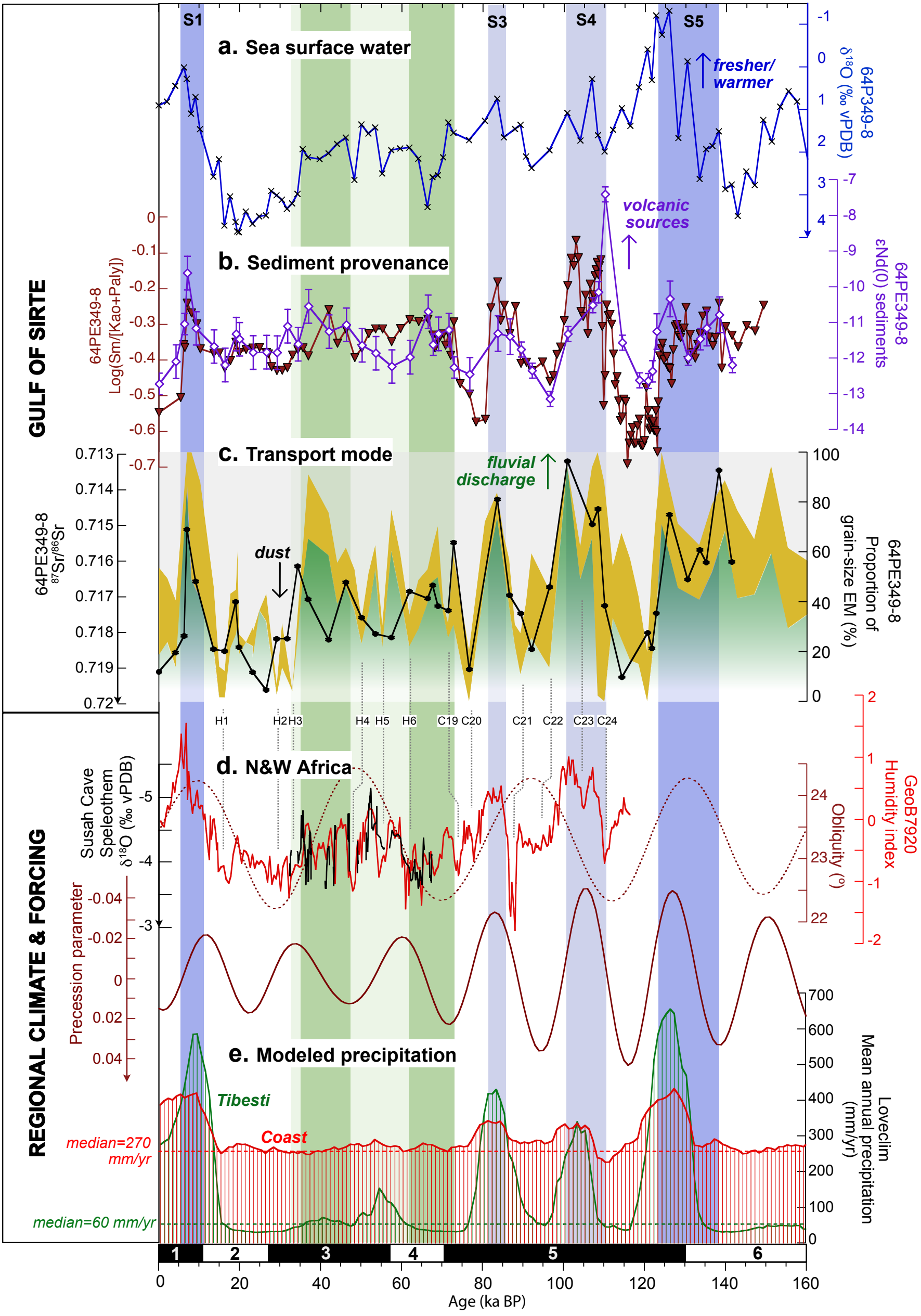
GULF OF SIRTE
REGIONAL CLIMATE & FORCING
S1
S3
S4
S5
a. Sea surface water
fresher/ warmer
64P349-8 δ18O (‰ vPDB)
b. Sediment provenance
volcanic sources
64PE349-8 Log(Sm/[Kao+Paly])
64PE349-8 εNd(0) sediments
c. Transport mode
fluvial discharge
dust
64PE349-8 87Sr/86Sr
64PE349-8 Proportion of grain-size EM (%)
H1
H2
H3
H4
H5
H6
C19
C20
C21
C22
C23
C24
d. N&W Africa
Susah Cave Speleothem δ18O (‰ vPDB)
Obliquity (°)
GeoB7920 Humidity index
Precession parameter
e. Modeled precipitation
Tibesti
Coast
median=270 mm/yr
median=60 mm/yr
Loveclim Mean annual precipitation (mm/yr)
1
2
3
4
5
6
Age (ka BP)

Figure 4

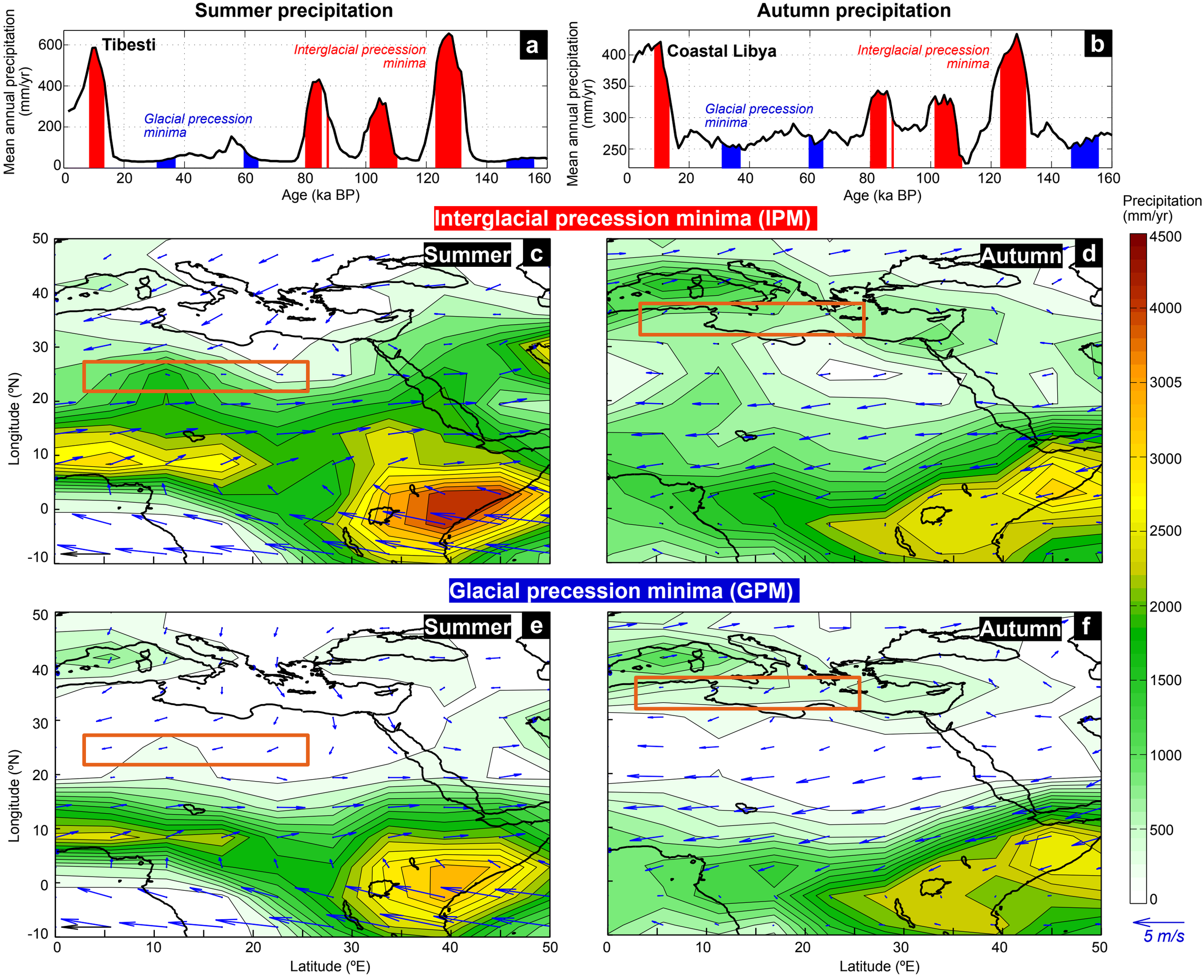
Summer precipitation
Tibesti
a
Interglacial precession minima
Glacial precession minima
Mean annual precipitation (mm/yr)
Age (ka BP)
Autumn precipitation
Coastal Libya
b
Interglacial precession minima
Glacial precession minima
Mean annual precipitation (mm/yr)
Age (ka BP)
Interglacial precession minima (IPM)
Summer
c
Autumn
d
Glacial precession minima (GPM)
Summer
e
Autumn
f
Longitude (°N)
Latitude (°E)
Precipitation (mm/yr)
5 m/s